Bifurcation analysis of optically induced dynamics in nematic liquid crystals: elliptical polarization at normal incidence

D. O. Krimer and L. Kramer*

Physikalisches Institut der Universität Bayreuth, D-95440 Bayreuth, Germany

E. Brasselet, T. V. Galstian,† and L. J. Dubé‡

Département de Physique, de Génie Physique, et d'Optique, Université Laval, Cité Universitaire, Québec, Canada G1K7P4

Received December 10, 2004; revised manuscript received February 15, 2005; accepted February 28, 2005

We present a detailed bifurcation analysis of the nonlinear reorientation dynamics of a homeotropically aligned nematic liquid-crystal film excited by an elliptically polarized beam at normal incidence with the intensity and the polarization state of light as the control parameters. The asymmetry arising from the elliptical polarization of the excitation lightwave is shown to affect dramatically the dynamics, and various new dynamical behaviors are reported: (i) quasi-periodic rotations for almost circular polarization; (ii) a discontinuous transition, identified as a homoclinic bifurcation, to a largely reoriented state over a large range of ellipticity values; (iii) oscillations associated with large reorientation; and (iv) optical multistability between several distinct dynamical regimes. © 2005 Optical Society of America

OCIS codes: 190.0190, 160.3710.

1. INTRODUCTION

Over the past two decades the effects associated with the propagation of laser light in a liquid crystal have been studied intensively.[1–4] The long-range orientational order of the molecules in these media adds a collective character to the light–matter interaction and generates a unique spatiotemporal feedback mechanism responsible for the rich dynamics of the optically induced orientational phenomena reported thus far.[5–10] A further attractive feature of these systems is that a rigorous theoretical framework [at least for nematic liquid crystals[11] (NLCs)] is available, involving Maxwell's equations together with the hydrodynamic equations of the liquid crystal. The description involves primarily the dynamics of the director **n**, a unit vector that designates the local axis of average orientation of the molecules.

Several interaction geometries involving polarized light and a homeotropic film of NLC (i.e., the molecules are perpendicular to the cell substrates) have received much attention ever since the discovery of the optical Fréedericksz transition (OFT) by Zolot'ko *et al.*[12] The system exhibits complex nonlinear dynamics accessible both experimentally and theoretically. Some of the cases treated are circular polarization (CP) excitation[13–17] and elliptical polarization (EP) excitation,[18,19] both at normal incidence; ordinary linearly polarized light at small oblique incidence[5–8,20–24]; and excitation with an elliptical intensity profile.[24,25]

The present paper is devoted to a detailed theoretical analysis of the role played by the anisotropy of the excitation during the reorientation dynamics in the EP case [see Fig. 1(a)]. The complete bifurcation scenario is obtained as a function of the excitation intensity and the ellipticity of the incoming light (for not-too-small ellipticities). In particular, it is shown that new dynamical regimes, not present in previous studies,[18,19] are expected. We can mention the quasi-periodic rotation regimes for almost CP; the discontinuous transition, identified as a homoclinic bifurcation,[26–28] to a largely reoriented state over a large range of ellipticity values; oscillations within this largely reoriented state; and optical multistability between several distinct dynamical regimes. Whenever possible, the theoretical results have been supported by experimental observations.

For our purpose, we introduce the normalized intensity $\rho = I/I_F^{\mathrm{CP}}$, where I is the excitation intensity and I_F^{CP} is the threshold intensity for the OFT under CP excitation (note that in Ref. 19 the intensity threshold for linear polarization $I_F^{\mathrm{LP}} = I_F^{\mathrm{CP}}/2$ was used for the normalization). The ellipticity angle χ ($-\pi/4 \leqslant \chi \leqslant \pi/4$) is related to the ratio between the minor (b) and the major (a) axes of the polarization ellipse by $\tan\chi = \pm b/a$ such that the incident beam carries an average angular momentum $\hbar \sin 2\chi$ per photon. The case $\chi = 0$ ($\chi = \pm\pi/4$) corresponds to a linearly (circularly) polarized excitation beam, and intermediate values refer to EP. Because the sign of χ determines the handedness of the polarization and hence the sense of rotation of the director around the light wave vector, it is sufficient to consider positive values of χ only.

The paper is organized as follows. Section 2 summarizes the theoretical and experimental background related to the present study. The theoretical bifurcation diagram in the plane of parameters (χ, ρ) is presented in Section 3 in which the comparison with previous studies

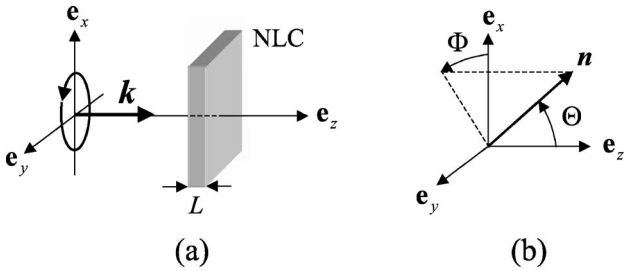

Fig. 1. (a) Interaction geometry in the Cartesian coordinate system (x,y,z), where $\mathbf{k}$ is the wave vector of the elliptically polarized excitation light, NLC is the nematic liquid-crystal film, and L is the cell thickness. (b) Representation of the director $\mathbf{n}=(\sin\Theta\cos\Phi,\sin\Theta\sin\Phi,\cos\Theta)$ in terms of the standard spherical angles Θ and Φ.

is made. In Section 4, the principal dynamical regimes are studied separately, and the transitions between them are discussed. Finally, our conclusions are summarized in Section 5.

2. GENERAL BACKGROUND

A. Theory

We choose a Cartesian coordinate system (x,y,z) with the z axis along the direction of the wave vector k of light [Fig. 1(a)]. The calculations are developed in the infinite-plane-wave approximation, justified if the spot size of the excitation beam is significantly larger than the thickness L of the NLC film. Under this assumption, all the relevant functions depend solely on the spatial coordinate z and time t. For convenience, we also introduce the normalized spatial coordinate ξ and time τ according to $\xi=z/L$ and $\tau=t/\tau_{\mathrm{NLC}}$, where L is the cell thickness and $\tau_{\mathrm{NLC}}=\gamma_1 L^2/\pi^2 K_3$ is a characteristic director reorientation time, with γ_1 as the rotational viscosity and K_3 as the bend elastic constant of the NLC.[11] The director representation $\mathbf{n}=(\sin\Theta\cos\Phi,\sin\Theta\sin\Phi,\cos\Theta)$ [Fig. 1(b)] associated with the homeotropic boundary conditions $\Theta(0,\tau)=\Theta(1,\tau)=0$ and $\partial_\xi\Phi(0,\tau)=\partial_\xi\Phi(1,\tau)=0$ suggests the expansion of angles Θ and Φ in an appropriate set of orthogonal functions[29]:

$$\Theta(\xi,\tau) = \sum_{n=1}^{\infty}\Theta_n(\tau)\sin(n\pi\xi), \tag{1}$$

$$\Phi(\xi,\tau) = \Phi_0(\tau)+\sum_{n=1}^{\infty}\Phi_n(\tau)\frac{\sin[(n+1)\pi\xi]}{\sin(\pi\xi)}. \tag{2}$$

The mode $\Phi_0(\tau)$ does not depend on ξ and describes the pure rotation of the director around the z axis. In the absence of a velocity field, the dynamical equations for the angles $\Theta(\xi,\tau)$ and $\Phi(\xi,\tau)$ are obtained from the balance between the torques (elastic, electromagnetic, and viscous) acting on the NLC. These individual torques are calculated from the variational derivatives of the elastic and the electromagnetic free-energy densities and the dissipation function density, respectively.[30] The resulting coupled equations can be written schematically as

$$\frac{\partial\Theta}{\partial\tau} = \mathcal{L}_\Theta(\xi,\tau), \tag{3}$$

$$\frac{\partial\Phi}{\partial\tau} = \mathcal{L}_\Phi(\xi,\tau), \tag{4}$$

where the expressions of the operators $\mathcal{L}_\Theta$ and $\mathcal{L}_\Phi$ are explicitly given by Eqs. (A1) in Ref. 31. The equations for each amplitude $\Theta_n(\tau)$ and $\Phi_n(\tau)$ are then obtained by projecting Eqs. (3) and (4) onto each mode according to

$$\frac{\mathrm{d}\Theta_n}{\mathrm{d}\tau} = 2\int_0^1\mathcal{L}_\Theta(\xi,\tau)\sin(n\pi\xi)\mathrm{d}\xi, \tag{5}$$

$$\frac{\mathrm{d}\Phi_n}{\mathrm{d}\tau} = 2\int_0^1\mathcal{L}_\Phi(\xi,\tau)\sin[(n+1)\pi\xi]\sin(\pi\xi)\mathrm{d}\xi. \tag{6}$$

The resulting infinite-dimensional integrodifferential problem is made tractable by truncation, leading to a finite-dimensional system for the angles $(\Theta_1,\ldots,\Theta_N;\Phi_0,\Phi_1,\ldots,\Phi_M)$. Finally, the resulting set of $N+M+1$ time-dependent Eqs. (5) and (6) is solved simultaneously with the equations governing the optical fields [see Eqs. (A4) in Ref. 31]. One retains a sufficient number of modes (N,M) to ensure approximation of the results within a given tolerance.

One point to emphasize is that, in the EP case and in contrast to the CP case, the equation for Φ_0 is coupled with the other equations. This is due to the broken rotational invariance around the z axis. A regime of simple rotation of the director (when $\mathrm{d}\Phi_0/\mathrm{d}\tau=$const. and $\mathrm{d}\Phi_n/\mathrm{d}\tau=\mathrm{d}\Theta_n/\mathrm{d}\tau=0$), possible in the CP case, cannot be realized when $\chi\neq\pi/4$. In the EP case, all modes (including Φ_0) are either time dependent ($\mathrm{d}\Phi_0/\mathrm{d}\tau\neq0$, $\mathrm{d}\Phi_n/\mathrm{d}\tau\neq0$, $\mathrm{d}\Theta_n/\mathrm{d}\tau\neq0$) or time independent ($\mathrm{d}\Phi_0/\mathrm{d}\tau=\mathrm{d}\Phi_n/\mathrm{d}\tau=\mathrm{d}\Theta_n/\mathrm{d}\tau=0$) simultaneously.

We may introduce the vector $\mathbf{x}=(\Theta_1,\ldots,\Theta_N,\Phi_0,\ldots,\Phi_M)$, rewriting Eqs. (5) and (6) as $\dot{\mathbf{x}}=\mathbf{F}(\mathbf{x})$ (the dot denotes the time derivative). It is clear that when all modes are time independent the problem is significantly simplified. In fact, instead of solving a system of evolution equations for $\mathbf{x}$, we are faced with a set of nonlinear algebraic equations $\mathbf{F}(\mathbf{x})=0$, which is done by a Newton–Raphson method. Its solution $\mathbf{x}_{\mathrm{D}}(\rho)$ represents a stationary distorted (D) state at some fixed value of ρ. Then the neighboring D state for $\rho+\delta\rho$ can be obtained by solving $\mathbf{F}(\mathbf{x})=0$ by using $\mathbf{x}_{\mathrm{D}}(\rho)$ as the initial guess. The operation is then repeated to obtain the solution $\mathbf{x}_{\mathrm{D}}$ for any ρ. Furthermore, one can easily perform the linear stability analysis of the D state by calculating the eigenvalues of the corresponding Jacobian matrix $J_{ij}=(\partial F_i/\partial x_j)_{\mathbf{x}=\mathbf{x}_{\mathrm{D}}}$.

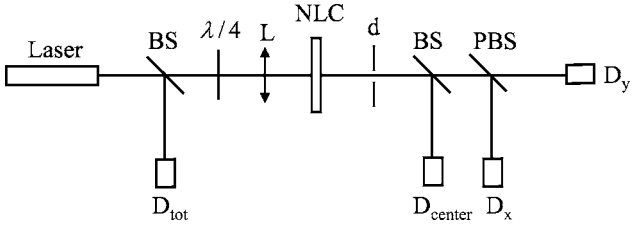

Fig. 2. Experimental setup. Laser, Verdi laser (from Coherent) operating at 532 nm; BS, beam splitter; λ/4, quarter-wave plate; L, lens; d, diaphragm; PBS, polarizing beam splitter; D_i, photodetectors.

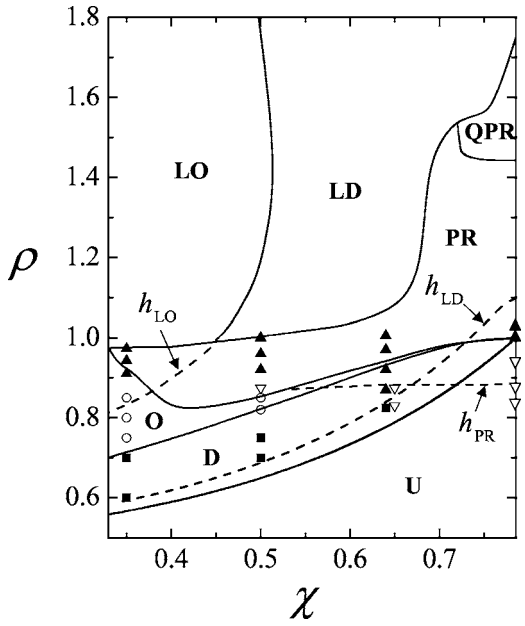

Fig. 3. Phase diagram of the dynamical regimes in the plane of parameter (χ,ρ). U, undistorted state; D, stationary distorted states; O, periodic oscillating states; PR, periodic rotating states; QPR, quasi-periodic rotating states; LD and LO, large reorientation associated, respectively, with stationary distorted and oscillating states. The dashed curves h_{PR}, h_{LD}, and h_{LO} correspond to the hysteretic region of the PR, LD, and LO states, respectively. The points are experimental data extracted from Ref. 19 for D (squares), O (circles), PR (triangles), and hysteretic PR (inverse triangles).

In addition, we introduce the phase delay $\Delta(\tau)$ defined as

$$\Delta(\tau) = \kappa_0 \int_0^1 [n_e(\xi,\tau) - n_o] \mathrm{d}\xi, \tag{7}$$

where $\kappa_0 = 2\pi L/\lambda$ is the normalized wave vector of the incident light with wavelength λ. Here $n_e(\xi,\tau) = n_o n_E / [n_E^2 \cos^2 \Theta(\xi,\tau) + n_o^2 \sin^2 \Theta(\xi,\tau)]^{1/2}$ is the extraordinary refractive index with n_o and n_E as the eigenordinary and eigenextraordinary refractive indices. $\Delta(\tau)$ corresponds therefore to the total phase shift between the *e* and *o* waves at the output ($\xi=1$) of the NLC cell if the light propagation is considered adiabatic through the reoriented NLC (i.e., in the so-called Mauguin regime). This phase has an experimental counterpart in that the quantity $\Delta/2\pi$ roughly represents the number of self-diffraction rings in the far field.[32]

For the sake of consistency, the same material parameters as in a companion paper[31] are used in the following calculations.

B. Experiment

Our experimental apparatus (Fig. 2) gives simultaneous access to the dynamical behavior of the polar (Θ) and the azimuthal (Φ) parts of the molecular configuration. This technique is described in Ref. 33. It consists of a Verdi laser (from Coherent) operating at 532 nm, whose linear polarization is made elliptical by using a quarter-wave plate. We adjust the ellipticity angle χ by rotating the quarter-wave plate and measuring the third normalized Stokes parameter $S_3 = \sin 2\chi$ by using a polarimeter (not shown in the figure). This beam is then focused on the NLC cell with a lens of focal length $f = 150$ mm.

Table 1. Calculated Sequence of Bifurcations as a Function of the Ellipticity χ of the Excitation Light[a]

Ellipticity	Sequence of Transitions	Bifurcation Nature
$0.33 < \chi < 0.53$	Unperturbed → distorted	Pitchfork
	Distorted → periodic oscillation	Supercritical Hopf
	Periodic oscillation → periodic rotation	Gluing
	Periodic rotation → periodic oscillation or distorted	Homoclinic[b]
$0.53 < \chi < 0.72$	Unperturbed → distorted	Pitchfork
	Distorted → periodic oscillation	Supercritical Hopf
	Periodic oscillation → periodic rotation−1	Gluing
	Periodic rotation−1 → periodic rotation−2	Saddle node
	Periodic rotation−2 → distorted	Homoclinic[c]
$0.72 < \chi < \pi/4$	Unperturbed → distorted	Pitchfork
	Distorted → periodic oscillation	Supercritical Hopf
	Periodic oscillation → periodic rotation−1	Gluing
	Periodic rotation−1 → periodic rotation−2	Saddle node
	Periodic rotation−2 → quasi-periodic rotation	Supercritical Hopf
	Quasi-periodic rotation → distorted or periodic rotation	Homoclinic[d]
$\chi = \pi/4$	Unperturbed → periodic rotation	Subcritical Hopf
	Periodic rotation → quasi-periodic rotation	Supercritical Hopf
	Quasi-periodic rotation → periodic rotation	Homoclinic[d]

[a] $\delta\alpha/\alpha$ refers to the relative jump of the quantity $\alpha = \Delta/2\pi$ experienced at the homoclinic bifurcation.

[b] $\delta\alpha/\alpha < 0.1$.

[c] $\delta\alpha/\alpha < 0.1$ for $\chi < 0.66$ and $\delta\alpha/\alpha \sim 10$ for $\chi > 0.66$.

[d] $\delta\alpha/\alpha \sim 10$.

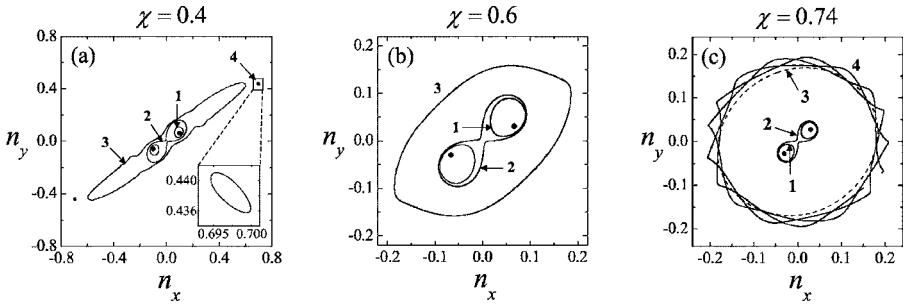

Fig. 4. Calculated director trajectories in the (n_x, n_y) plane. (a) $\chi=0.4$: stationary distorted state (D) at $\rho=0.72$ (filled circles); periodic oscillating state (O) at $\rho=0.76$ (curve 1); periodic rotating state (PR) just above the gluing bifurcation at $\rho=0.83$ (curve 2) and slightly below the transtion to the largely reoriented oscillating state (LO) at $\rho=0.97$ (curve 3); largely reoriented oscillating state at $\rho=0.98$ (curve 4, see inset). (b) $\chi=0.6$: stationary distorted state (D) at $\rho=0.8$ (filled circles); periodic oscillating state (O) at $\rho=0.91$ (curve 1); periodic rotating state PR_1 slightly above the gluing bifurcation at $\rho=0.917$ (curve 2); periodic rotating state PR_2 at $\rho=0.95$ (curve 3). (c) $\chi=0.74$: stationary distorted state (D) at $\rho=0.99$ (filled circles); periodic oscillating state (O) at $\rho=0.9925$ (curve 1); periodic rotating state PR_1 slightly above the gluing bifurcation at $\rho=0.9932$ (curve 2); periodic rotating state PR_2 slightly above the saddle-node bifurcation at $\rho=0.9936$ (curve 3, dashed curve); quasi-periodic rotating state at $\rho=1.5$ (curve 4).

The beam diameter is $2w_0=30$ μm at the sample location, and the cell thickness is $L=75$ μm. The director dynamics is retrieved by the analysis of the central part of the emerging beam after the diaphragm d. Photodiodes D_{center}, D_x, and D_y collect, respectively, the total intensity of the central part of the beam, I_{center}, and the intensities, I_x and I_y, of the x and y electric field components ($I_{\text{center}}=I_x+I_y$). The incident intensity I_{tot} is monitored by the photodiode D_{tot}. The data-acquisition frequency is 4 Hz. The behavior of the signal $I_{\text{center}}(\tau)$ is qualitatively similar to that of $\Delta(\tau)$, whereas the behavior of the signals $i_x(\tau)\equiv I_x/I_{\text{center}}$ and $i_y(\tau)\equiv I_y/I_{\text{center}}$ can be compared with the calculated intensities at the output of the sample, $I_x(\tau)=|E_x(\xi=1,\tau)|^2$ and $I_y(\tau)=|E_y(\xi=1,\tau)|^2$, respectively. Because $i_x(\tau)=1-i_y(\tau)$, these time series possess the same dynamical information, and we shall refer to any of these quantities as $i(\tau)$.

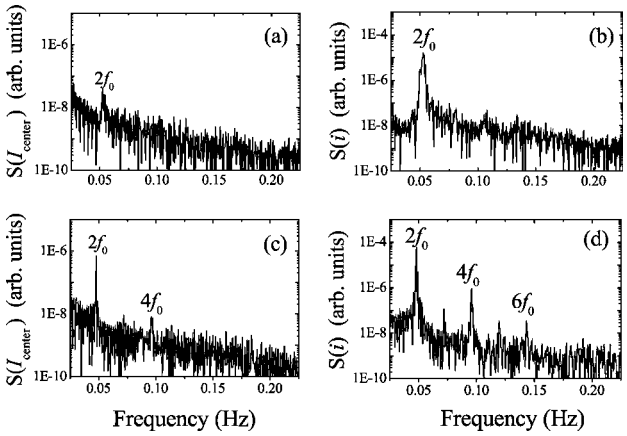

Fig. 5. Experimental power spectra $\mathcal{S}(I_{\text{center}})$ and $\mathcal{S}(i)$ in the periodic rotating regime for $\rho=1.10$ and (a), (b) $\chi\approx\pi/4$ and (c), (d) $\chi=0.74$.

3. BIFURCATION SCENARIO

In this section, the director dynamics is analyzed by taking ρ and χ as control parameters. The results are presented for ellipticity values in the range $0.33\leqslant\chi\leqslant\pi/4$, for which transitions between different dynamical regimes are observed. For lower values of χ the rotating states (see below) do not exist, and some aspects of the scenario in that region can be found in Refs. 18,19.

A. Phase Diagram of the Regimes and Bifurcations

Figure 3 presents the different regimes that exist in the (χ,ρ) plane for $0.33\leqslant\chi\leqslant\pi/4\simeq0.785$. Experimental data points extracted from Ref. 19 are also indicated. Below the OFT threshold that depends on χ as $I_F^{\text{EP}}=I_F^{\text{CP}}/(1+\cos 2\chi)$,[30] the director is unperturbed (U). Above the threshold, several regimes can exist depending on the values of χ and ρ: stationary distorted (D), oscillating (O), periodic rotating (PR), quasi-periodic rotating (QPR), and largely reoriented states ($\Theta\sim1$), which may be stationary distorted (LD), oscillating (LO), or rotating (LR) states (LR states are not shown on Fig. 3 in that they arise only in a narrow region $\Delta\chi\sim10^{-2}$ near $\chi=\pi/4$, as discussed in Subsection 4.E). Keeping the ellipticity fixed and increasing the intensity, we see that these regimes appear as a well-defined sequence of transitions. In the range of interest for χ, several distinct bifurcation sequences can be identified. These results are summarized in Table 1, and the trajectories of the director in the various regimes are shown in Fig. 4.[34] In what follows, the dependence of the detailed bifurcation scenario on the value of χ is presented for increasing values of χ.

For $0.33<\chi<0.53$, the OFT is a pitchfork bifurcation, and the reoriented state is a D state [see the filled circles in Fig. 4(a)]. This state loses its stability through a supercritical Hopf bifurcation to an O state [curve 1 in Figs. 4(a)] characterized by a single frequency f_0 (Table 2). The reflection symmetry is spontaneously broken by the primary bifurcation, so, in the D and O states, one has two symmetry-degenerate solutions related by $\{n_x\rightarrow-n_x,\ n_y\rightarrow-n_y\}$. As ρ increases, these two limit cycles merge in a gluing bifurcation at the origin and restore the reflection symmetry. This leads to the appearance of a single double-length limit cycle that corresponds to the trajectory in the PR state [curve 2 in Fig. 4(a)]. A further increase of the intensity eventually leads to a discontinuous transition to a largely reoriented oscillating ($\chi<0.45$) or stationary distorted ($\chi>0.45$) state. In both cases this transition is associated with a small relative jump $\delta\alpha/\alpha$ of

Table 2. Spectral Content of $n_{x,y}(\tau)$, $I_{x,y}(\tau)$, and $\Delta(\tau)$ for the Different Dynamical Regimes for an Elliptically Polarized Excitation

Regime	$n_{x,y}$	$I_{x,y}$	Δ
Periodic oscillation (O)	nf_0	nf_0	nf_0
Periodic rotation (PR)	$(2n-1)f_0$	$2nf_0$	$2nf_0$
Quasi-periodic rotation (QPR)	$nf_1 \pm (2m+1)f_0$	$nf_1 \pm 2mf_0$	$nf_1 \pm 2mf_0$

the quantity $\alpha=\Delta/2\pi$ (typically, $\delta\alpha/\alpha<0.1$) and corresponds to a homoclinic bifurcation (see Subsection 4.D). In fact, stable LO states exist until the intensity is decreased to a critical value represented by the hysteretic line h_{LO} in Fig. 3, below which the LO state becomes stationary distorted. This LD state finally vanishes when the intensity is decreased below the hysteretic line h_{LD}.

For $0.53<\chi<0.72$, one has the sequence U$\rightarrow$D$\rightarrow$O$\rightarrow$PR as before [see Fig. 4(b)]; however, there is an additional bifurcation between PR states. In fact, the limit cycle amplitude of the PR regime, now labeled PR_1 [curve 2 in Fig. 4(b)], abruptly increases. This results in another periodic rotating regime labeled PR_2 with higher reorientation amplitude [curve 3 in Fig. 4(b)]. This is a hysteric transition connected to a double saddle-node structure with the (unstable) saddle separating the PR_1 and PR_2 branches, as already discussed in Ref. 19. In that case, the system switches back to the O or D state at the line labeled h_{PR} in Fig. 3. In contrast, no hysteresis is observed when ρ is decreased starting from the PR_1 regime because the O$\rightarrow\mathrm{PR}_1$ transition is continuous. The $\mathrm{PR}_1\rightarrow\mathrm{PR}_2$ transition is not shown in Fig. 3 because it is very near to the gluing bifurcation. At $\chi=0.53$ the two saddle nodes coalesce. Finally, for high intensity the system abruptly switches from the PR_2 to the LD regime. The reorientation discontinuity associated with this transition is small for $\chi<0.66$ (typically, $\delta\alpha/\alpha<0.1$) and quite large for $\chi>0.66$ (typically, $\delta\alpha/\alpha\sim10$). As before, the transition to large reorientation is found to be a homoclinic bifurcation and, when the intensity is decreased, stable LD states exist until the line h_{LD} is reached.

For $0.72<\chi<\pi/4$ the sequence U$\rightarrow$D$\rightarrow$O$\rightarrow\mathrm{PR}_1\rightarrow\mathrm{PR}_2$ is observed as before [see Fig. 4(c)]. However, for higher values of ρ, a QPR regime is born through a secondary supercritical Hopf bifurcation, which introduces a new frequency f_1 into the system and transforms the dynamics into a quasi-periodic behavior [curve 4 in Fig. 4(c)]. As the intensity increases, the QPR state undergoes a homoclinic transition to a largely reoriented LD or LR regime, which is, respectively, represented by a stationary distorted or slowly rotating (close to $\chi=\pi/4$) state. This bifurcation is associated with a large discontinuity of the reorientation amplitude, namely, $\delta\alpha/\alpha\sim10$.

As mentioned earlier, the particular case $\chi=\pi/4$, i.e., CP excitation, has been the subject of a separate study, and we refer the interested reader to Ref. 31 for more details. In that case, one should note that the intensity value on the hysteretic line h_{LD} at $\chi=\pi/4$ corresponds to the intensity ρ_3^* introduced in Ref. 31. A summary of the results obtained there are presented at the end of Table 1.

The signature of the anisotropy of incident light is visible in the director trajectories in the (n_x,n_y) plane. The PR trajectories are obviously noncircularly symmetric for $\chi=0.4$ and $\chi=0.6$ [see Figs. 4(a) and 4(b)], whereas the PR_2 and QPR regimes are almost circularly symmetric when the polarization is almost CP [see Fig. 4(c)]. In addition, one recalls that the dynamical regimes O, PR, and QPR can be described by means of one (for O and PR regimes) or two (for the QPR regime) frequencies, f_0 and f_1. The spectral content of the variables $n_{x,y}$, Δ, and $I_{x,y}$ is listed in Table 2. In fact, a simple way of identifying a given dynamical regime is to look at the spectra of the relevant variables.

B. Comparison with Previous Studies

Our results may be compared with previous rigorous[18] and approximate[19] calculations. In Ref. 18, the equations of motion for the director were solved numerically, whereas in Ref. 19 they were solved by using the same mode expansion as we have used here [Eqs. (1) and (2)] but retaining only Θ_1 and the modes Φ_0 and Φ_1 (inclusion of additional twist modes $\Phi_{n\geqslant2}$ were shown not to qualitatively alter the dynamics). In contrast to our calculations, however, their coupled-mode equations have been solved approximately in the small distortion approximation. The QPR, LO, and LR regimes were not reported in both these approaches, although other dynamical regimes such as O and PR were obtained and observed experimentally.[18] Moreover, the homoclinic bifurcation from the PR to the LO or LD regime and the one from the QPR to the LD or LR regime was not found. Finally, we can mention that the nonlinear twist terms $[\propto(\partial_z\Phi)^2]$ were neglected in Ref. 19, suppressing the QPR regime, although asymmetric azimuthal modes were taken into account.

From an experimental point of view, the observation of the QPR state has been reported in the particular case of a CP excitation, and it has been ascribed to the competition from symmetric and asymmetric reorientation modes.[16] Concerning the O regime, it has been theoretically predicted to exist only below $\chi=0.6$ in Ref. 18, whereas it was shown to exist over a significant range of ρ in Ref. 19 until it vanishes at $\chi=\pi/4$. On the other hand, the oscillating states have not been observed for an ellipticity larger than $\chi=0.5$ (open circles in Fig. 3). This point is easily understood with a look at Fig. 3 in which the region of existence of the O regime appears small for χ

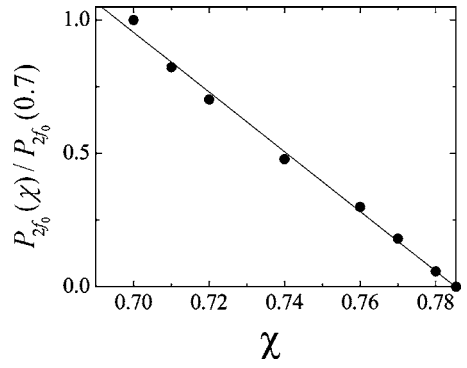

Fig. 6. Calculated amplitude of the fundamental peak $2f_0$ in $\mathcal{S}(\Delta)$ over the amplitude of the same peak at $\chi=0.7$ versus χ for $\rho=1.10$. The solid line is a linear fit.

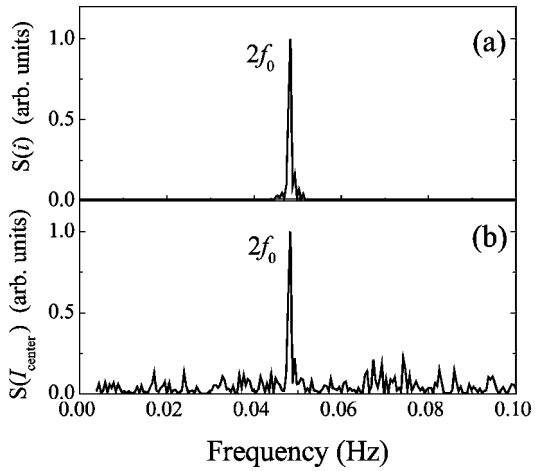

Fig. 7. Experimental power spectra (a) $\mathcal{S}(i)$ and (b) $\mathcal{S}(I_{\text{center}})$ in the periodic rotating regime for $\rho=1.10$ and $\chi=0.76$.

>0.5. For lower values of χ, the O regime exists for a significant range of intensities, a range that increases as χ is further decreased in agreement with observations.

4. DYNAMICAL REGIMES

We will now discuss more specifically some of the symmetry-breaking effects arising with the variation of the polarization state of the incident light, and we will present the corresponding experimental confirmation. In what follows, the Fourier power spectrum of a variable $X(\tau)$ is denoted by $\mathcal{S}(X)$.

A. Periodic Rotating Regime

When the system is in the PR state, all the spectra of the dynamical variables are described by a single frequency f_0 (and, for $\chi<\pi/4$, by its harmonics as well). More precisely, we expect from theory that both spectra $\mathcal{S}(I_{\text{center}})$ and $\mathcal{S}(i)$ exhibit harmonics $2nf_0$ at $\chi=0.74$, whereas a single frequency $2f_0$ should be present in $\mathcal{S}(i)$ at $\chi=\pi/4$.[31] The experimental results are shown in Fig. 5 in which $\mathcal{S}(I_{\text{center}})$ and $\mathcal{S}(i)$ are plotted at $\rho=1.10$ with $\chi\approx\pi/4$ [Figs. 5(a) and 5(b)] and $\chi=0.74$ [Figs. 5(c) and 5(d)].

From Figs. 5(a) and 5(b) we see that the observations agree almost perfectly with theory in the case of CP. However, a residual peak at the frequency $2f_0$ can be distinguished in $\mathcal{S}(I_{\text{center}})$. We believe this can be explained from the nonperfect rotational invariance around the z axis in the experiment. In fact, using a polarimeter we found that the angle χ satisfies $0.78\leqslant\chi\leqslant\pi/4$, i.e., within 1% or better accuracy of the ideal value $\pi/4$. From Figs. 5(a) and 5(c) the ratio between the maximum peak values at $2f_0$ in $\mathcal{S}(I_{\text{center}})$ for $\chi\approx\pi/4$ and $\chi=0.74$ is measured to be 0.047. On the other hand, Fig. 6 presents the theoretical ratio $P_{2f_0}(\chi)/P_{2f_0}(0.7)$ as a function of χ, where $P_{2f_0}(\chi)$ is the peak value at $2f_0$ in $\mathcal{S}(\Delta)$ at $\rho=1.10$ obtained by fitting each peak profile by a Lorentzian function. Finally, from Fig. 6, we find that the experimental ratio 0.047 corresponds to a theoretical estimate of $\chi=0.783$, which is consistent with the experimental uncertainty on χ.

When the incident light is almost circularly polarized, a satisfactory agreement is also observed as seen from Figs. 5(c) and 5(d) in which higher-order harmonics $(2nf_0, n\geqslant 2)$ are observed in both $\mathcal{S}(I_{\text{center}})$ $(n=2)$ and $\mathcal{S}(i)$ $(n=2$ and $n=3)$. However, residual peaks at the harmonics $n=3$ and $n=5$ can be distinguished in $\mathcal{S}(i)$ (the ratio between the maximum of two consecutive peaks is $P_{n=3}/P_{n=2}\sim 10^{-3}$ and $P_{n=5}/P_{n=4}\sim 5\times 10^{-2}$). The reason for this is not clear at present. The exact nature of these spectra obviously depends on χ and ρ. As χ approaches $\pi/4$, with ρ fixed, the calculations show that the relative weight of higher-order harmonics goes to zero and that the oscillation amplitude of $\Delta(\tau)$ goes also to zero (this trend is shown in Fig. 6). In addition, the amplitude of the harmonics decays quite rapidly with increasing n at fixed (χ,ρ), as illustrated in Fig. 5(d). These results help us understand why only the fundamental frequency $2f_0$ is observed at $\chi=0.76$ and $\rho=1.10$ (Fig. 7). In this case, the synchronous character of the precession (i.e., $\partial_t\Phi\neq 0$) and the nutation (i.e., $\partial_t\Theta\neq 0$) is almost perfectly verified despite a signal-to-noise ratio in $\mathcal{S}(i)$ of the order of $\sim 10\%$. This situation is about halfway between the results of Figs. 5(a) and 5(b) at $\chi=\pi/4$ and those of Figs. 5(c) and 5(d) at $\chi=0.74$.

B. Transition from Periodic Rotating Regime to Quasi-Periodic Rotating Regime

When $\chi>0.72$, the periodic rotating regime is predicted to lose its stability at $\rho=\rho_{\text{PR}\to\text{QPR}}$ (which depends on χ; see Fig. 3). The resulting director dynamics then becomes a quasi-periodic rotation characterized by two frequencies f_0 and f_1. This is illustrated in Figs. 8(c) and 8(d) in which $\mathcal{S}(\Delta)$ and $\mathcal{S}(I_{x,y})$ are calculated for $\chi=0.74$ and $\rho=1.50$. Although the PR$\to$QPR transition appears similar to the one observed in the CP case with regard to the generation of a new frequency f_1,[31] the spectral composition of the dynamical variables in the QPR state are different in the CP and the EP cases. This can be seen by comparing Figs. 8(a) and 8(b), taken at $\chi=\pi/4$ and $\rho=1.50$, with Figs. 8(c) and 8(d). Both $\mathcal{S}(\Delta)$ and $(I_{x,y})$ contain the frequencies $nf_1\pm 2mf_0$ in the EP case (see Table 2), whereas the spectral contents of the same quantities are given, respectively, by nf_1 and $nf_1\pm 2f_0$ in the CP case.[31] In other words,

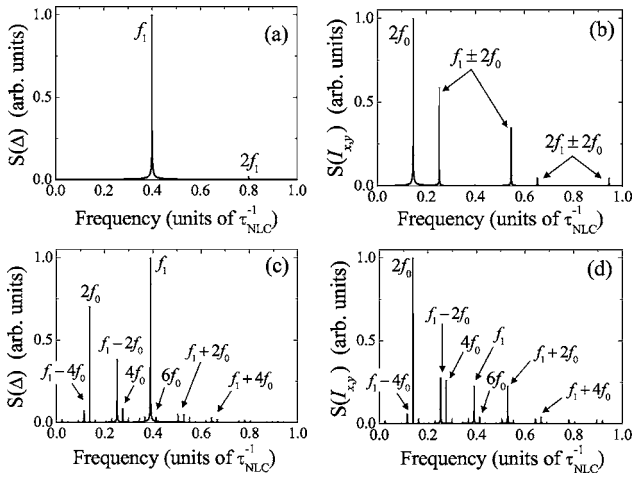

Fig. 8. Calculated power spectra $\mathcal{S}(\Delta)$ and $\mathcal{S}(I_{x,y})$ in the quasi-periodic rotating regime for $\rho=1.50$ at (a), (b) $\chi=\pi/4$ and (c), (d) $\chi=0.74$.

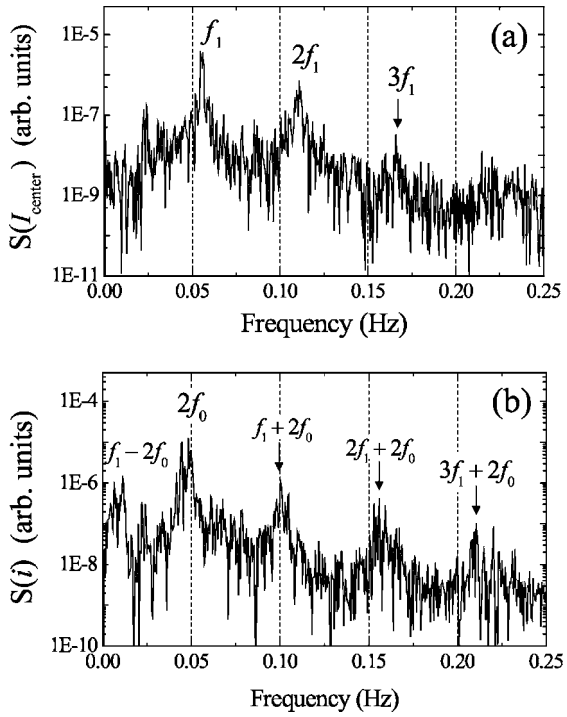

Fig. 9. Experimental power spectra (a) $\mathcal{S}(I_{\text{center}})$ and (b) $\mathcal{S}(i)$ in the quasi-periodic rotating regime for $\rho=1.30$ and $\chi=0.76$.

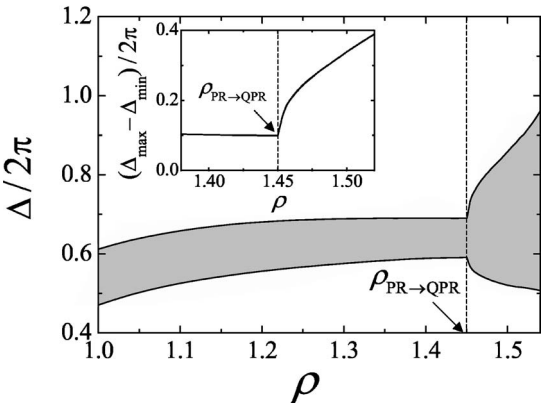

Fig. 10. Calculated $\Delta/2\pi$ versus ρ at $\chi=0.74$ showing the supercritical Hopf bifurcation from the periodic to the quasi-periodic rotating regime at $\rho=\rho_{\text{PR}\to\text{QPR}}$. The gray region represents the values explored during the oscillations of $\Delta(\tau)$. Inset: amplitude $\mathcal{A}=(\Delta_{\max}-\Delta_{\min})/2\pi$ characterizing the oscillation of $\Delta(\tau)$ in the neighborhood of the bifurcation point $\rho=\rho_{\text{PR}\to\text{QPR}}$.

both precession and nutation are quasi periodic in the EP case, whereas only precession is quasi periodic in the CP case.

We have observed experimentally the transition from the PR to the QPR regime, illustrated for $\chi=0.76$ below the threshold in Fig. 7 and above the threshold in Fig. 9. At the transition to quasi-periodic dynamics, the emergence of the new frequency f_1 and its harmonics changes dramatically the experimental spectra $\mathcal{S}(I_{\text{center}})$ and $\mathcal{S}(i)$ (Fig. 9). As predicted by theory, f_1 is the dominant frequency of $\mathcal{S}(I_{\text{center}})$ [Fig. 9(a)], and $2f_0$ is the dominant frequency of $\mathcal{S}(i)$ [Fig. 9(b)]. Recall that I_{center} (experimental) is related to Δ (theoretical) and i (experimental) is related to $I_{x,y}$ (theoretical).

We can further characterize the nature of the bifurcation at $\rho=\rho_{\text{PR}\to\text{QPR}}$ by verifying the scaling properties associated with the bifurcation. First, we have checked in the calculations that the amplitude of the limit cycle, $\mathcal{A}$, satisfies the scaling law $\mathcal{A}(\rho)-\mathcal{A}(\rho_{\text{PR}\to\text{QPR}})=\mathcal{O}(\rho-\rho_{\text{PR}\to\text{QPR}})^{1/2}$ in the neighborhood of the bifurcation point. For this purpose, we define theoretically this amplitude as $\mathcal{A}=(\Delta_{\max}-\Delta_{\min})/2\pi$, where $\Delta_{\max,\min}$ are, respectively, the maximum and the minimum of the oscillating phase delay $\Delta(\tau)$ for a given ρ. The results are shown in Fig. 10 in which $\mathcal{A}$ is plotted versus ρ. In the vicinity of the bifurcation, we find indeed that $\mathcal{A}(\rho)-\mathcal{A}(\rho_{\text{PR}\to\text{QPR}})=\mathcal{O}(\rho-\rho_{\text{PR}\to\text{QPR}})^{\gamma}$ with $\gamma\simeq 0.5$ and $\rho_{\text{PR}\to\text{QPR}}\simeq 1.45$. We have also verified that the frequency f_1 satisfies the scaling law $f_1(\rho)-f_1(\rho_{\text{PR}\to\text{QPR}})=\mathcal{O}(\rho-\rho_{\text{PR}\to\text{QPR}})$ as one can see from Fig. 11(b). Together, these results confirm that there is a secondary supercritical Hopf bifurcation at $\rho=\rho_{\text{PR}\to\text{QPR}}$.

C. Quasi-Periodic Rotating Regime

The dependence of the frequencies f_0 and f_1 as a function of the excitation intensity is displayed in Fig. 11 for different values of χ: $\chi=\pi/4$ (curve 1), $\chi=0.75$ (curve 2), and $\chi=0.73$ (curve 3). The frequency f_0 is obtained from the calculation of $\mathcal{S}(I_{x,y})$, which exhibits the dominant frequency $2f_0$. On the other hand, in the QPR regime, the frequency f_1 is extracted from $\mathcal{S}(\Delta)$, where it is the dominant frequency [see Figs. 8(c) and 9(a)].

The transition PR$\to$QPR is associated with an abrupt change of the slope of the precession frequency f_0 versus intensity [see Fig. 11(a)]. This can be rephrased as follows. In the QPR regime, the phase shift Δ explores values closer to 2π as ρ increases (Fig. 10), and the total angular-momentum transfer per photon to the NLC, $(1-\cos\Delta)\hbar$, is correspondingly smaller. Figures 11(a) and 11(b) show that a decrease of the ellipticity at fixed intensity corresponds to a decrease of both f_0 and f_1. The de-

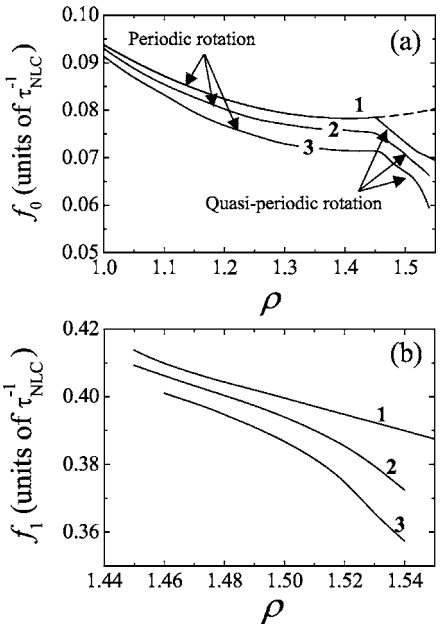

Fig. 11. Calculated characteristic frequencies (a) f_0 and (b) f_1 versus ρ in the periodic and quasi-periodic rotating regime for $\chi=\pi/4$ (curve 1), $\chi=0.75$ (curve 2) and $\chi=0.73$ (curve 3).

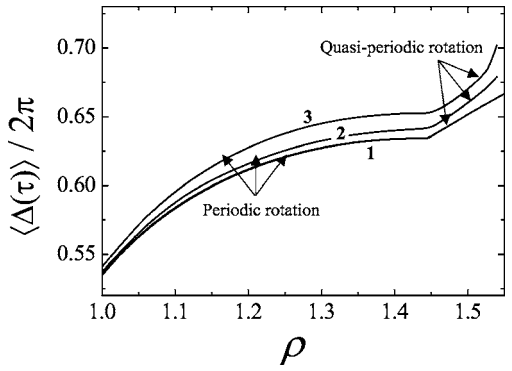

Fig. 12. Calculated temporal mean value $\langle\Delta(\tau)\rangle$ of $\Delta(\tau)$ divided by 2π versus ρ in the periodic and quasi-periodic rotating regimes for $\chi=\pi/4$ (curve 1), $\chi=0.75$ (curve 2), and $\chi=0.73$ (curve 3).

crease of f_0 is related to the fact that the temporal mean value $\langle\Delta(\tau)\rangle$ of $\Delta(\tau)$ at fixed ρ gets closer to 2π as χ decreases (see Fig. 12).

D. Transition from Periodic or Quasi-Periodic Rotating Regime to the Largely Reoriented Regime

Starting from the PR or QPR regime and increasing the intensity, we find that an instability eventually occurs at $\rho=\rho_L$ (which depends on χ; see Fig. 3), and the director settles to a largely reoriented oscillating (LO), stationary distorted (LD), or rotating (LR) state. As previously mentioned in Subsection 3.A, the LR regime exists only in a narrow region $\Delta\chi\sim10^{-2}$ around $\chi=\pi/4$ and is not seen in Fig. 3 (see Subsection 4.E). From Fig. 3 we see that the final state above ρ_L is a LO state if $\chi<0.45$ and a LD state if $\chi>0.45$. We find that the transition from the PR or QPR regime to the largely reoriented states is related to an increase of the period of the corresponding limit cycle. More precisely, this period appears to diverge logarithmically at $\rho=\rho_L$. This behavior is illustrated in Fig. 13 for $\chi=0.57$, where we find the bifurcation at $\rho_L=1.02025\ldots$. In this figure, the period $T=1/(2f_0)$ of the instantaneous angular velocity $\Omega(\tau)=d\Phi_0/d\tau$ is plotted as a function ρ (the factor $\frac{1}{2}$ in the expression of T is introduced owing to the π invariance around the z axis). A perfect agreement with the calculated values (filled circles) is obtained with the parameterization $a+b\ln(\rho_L-\rho)$ for $a\simeq8.232$ and $b\simeq-2.406$ (solid curve). The origin of this critical slowing down near the bifurcation point is illustrated in Fig. 14, where the director trajectory in the (n_x,n_y) plane is shown. Slightly below ρ_L ($\rho=1.02025$, black solid curve on the left) the trajectory approaches a saddle fixed point (filled square) during increasingly long times; this corresponds to the plateau behavior when $\Omega\sim0$ in the inset of Fig. 13. On the other hand, slightly above ρ_L ($\rho=1.02026$, gray curve in Fig. 14), the director eventually settles to a stable focus (filled circle) that corresponds to a LD state.[35] The nature of the singularity at $\rho=\rho_L$ guarantees that the transition has the character of a homoclinic bifurcation.[26–28] In fact, we deal here with a homoclinic bifurcation of the simplest type in which a limit cycle collides with a saddle point having only one unstable direction (all the eigenvalues have negative real parts except one, which is real and positive).

As already introduced in Subsection 3.A, a characteristic feature of the homoclinic bifurcation is that the transition is accompanied by a small relative jump of the reorientation amplitude for $\chi<0.66$ (typically, $\delta\alpha/\alpha<0.1$), whereas for $\chi>0.66$ it is quite large (typically, $\delta\alpha/\alpha\sim10$). This behavior is related to the fact that, for $\chi<0.66$, part of the limit cycle, associated with the PR state just below the transition, extends to large reorientations in the (n_x,n_y) plane. Consequently, it is already close to the largely reoriented states nearby [see, e.g., curves 3 and 4 in Fig. 4(a)].

Finally, one should mention the particular situation when the PR regime vanishes at $\chi=0.33$ (see Fig. 3). There, a direct transition from the O to the LO regime occurs as the intensity is increased. The corresponding picture is this: As the intensity is increased, the limit cycle associated with the O regime collides with an unstable fixed point, thus preempting the gluing at the origin. This dynamical sequence suppresses the appearance of the PR regime.

E. Transition between Largely Reoriented States

When the excitation beam is circularly polarized ($\chi=\pi/4$), it is already known that a LR state appears at high intensities.[15] This slow dynamics is quite fragile and disappears for perturbation of the ellipticity as small as $\Delta\chi\sim10^{-2}$, giving rise to a LD regime instead. With sufficient care, however, its experimental observation is possible[36] because the value of χ can be controlled with great accuracy. The mechanism for the disappearance of the LR regime is the following. In the CP limit, the precession frequency associated with the LR state exhibits almost periodic modulation as a function of the intensity with zero minimum values (see Fig. 3 of Ref. 15). As soon as the ellipticity is reduced, we find that the points of zero frequency transform into finite regions that continue to increase as χ is further decreased. Eventually, these regions join, leading to the LR→LD transition.

In the region of largely reoriented states, the LO regime appears for $\chi<0.51$ (see Fig. 3). This state is characterized in the (n_x,n_y) plane by a limit cycle with a small radius [see curve 4 in Fig. 4(a)]. Because of the presence

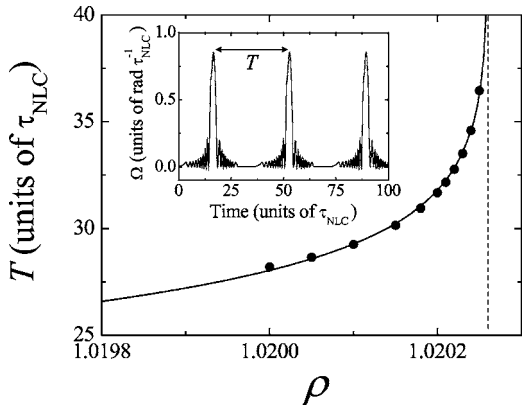

Fig. 13. Characterization of the homoclinic bifurcation near ρ_L for $\chi=0.57$, $T(\rho)=\mathcal{O}[\ln(\rho_L-\rho)]$, where T is the period of the instantaneous angular velocity $\Omega(\tau)=d\Phi_0/d\tau$. The solid curve is the best fit to the theoretically calculated values (circles). Inset: time evolution of $\Omega(\tau)$ at $\rho=1.02025$.

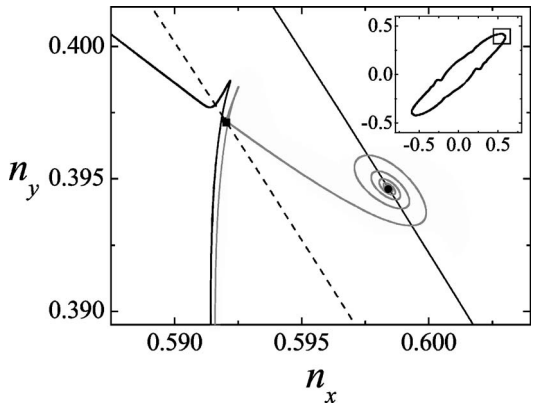

Fig. 14. Director trajectory in the (n_x,n_y) plane near the homoclinic bifurcation point ρ_L at $\chi=0.57$. Inset: homoclinic PR trajectory slightly below ρ_L ($\rho=1.02025$). Main graph: magnification of the region delimited by the box in the inset. The black solid curve on the left is part of the PR trajectory at $\rho=1.02025$, and the gray curve is the transient trajectory converging to a stable fixed point just above ρ_L ($\rho=1.02026$). The dashed line (solid line on the right) represents the location of the unstable (stable) fixed points in a small range of ρ centered around ρ_L. The filled square and filled circle represent, respectively, the unstable and the stable fixed point at $\rho=1.02025$ and $\rho=1.02026$.

of multistability, the boundary between the LD and the LO regimes in the (χ,ρ) plane demands careful attention. To obtain this locus, we have proceeded as follows. First, for a fixed $\chi>0.45$ and starting from the PR regime, we slowly increase ρ, and we find the LD state to which the system settles as we cross the transition at $\rho=\rho_L$. This is done by integrating the set of Eqs. (5) and (6) over a time duration much larger than any transients until a stable fixed point solution is obtained. Figure 14 illustrated this procedure: Slightly above ρ_L, a portion of a transient trajectory (gray curve) is seen to converge to a stable fixed point indicated by a filled circle. Next, we follow the LD states for $\rho>\rho_L$ according to the procedure described in Subsection 2.A: The solid line on the right of Fig. 14 shows the result for $\chi=0.57$. By performing the linear stability analysis of these LD states, we can finally conclude that the LD states (which were stable at $\rho=\rho_L$) lose their stability at some higher value of ρ in the range $0.45<\chi<0.51$, leading to a LO state. In fact, the transition LD $\rightarrow$LO takes place via a Hopf bifurcation. Moreover, these unstable LD states eventually recover their stability at higher intensities leading to the inverse transition LO $\rightarrow$LD.

5. CONCLUSION

The nonlinear reorientation dynamics generated by elliptically polarized light at normal incidence to a homeotropic nematic liquid-crystal film has been investigated. In particular, the dramatic sensitivity of the dynamics on rotational symmetry breaking has been discussed on the basis of experimental observations and theoretical predictions. The complete bifurcation diagram with the light intensity and the ellipticity as control parameters has been calculated rigorously. We have found that a quasi-periodic regime extends from the circular to the elliptical polarization excitations down to the value $\chi=0.72$. However, in the elliptical case, the spectra of the dynamical variables become more complicated than in the circular case, although they are still characterized by two distinct frequencies associated with precession and nutation. As in the circular case, the quasi-periodic states appear via a secondary supercritical Hopf bifurcation, and experimental observations have confirmed the existence of the quasi-periodic regime. In addition, we have found a new dynamical regime that corresponds to an oscillating regime with large reorientation for ellipticity values lower than $\chi=0.51$. More generally, the transition from the periodic or the quasi-periodic rotating regime to a largely reoriented rotating, oscillating, or distorted regime has been identified as an homoclinic bifurcation in which a limit cycle collides with a saddle point. The different transitions between these different states associated with large molecular reorientation and their hysteretic behavior when the intensity is decreased have also been identified.

These results reinforce the surprisingly rich nature of the molecular reorientation dynamics driven by the transfer of spin angular momentum of light in liquid crystals materials.

We thank A. Vella and E. Santamato for information concerning their work. E. Brasselet, D. O. Krimer, and L. Kramer acknowledge financial support by the Deutsche Forschungsgemeinschaft under Kr 690/16, 436UNG113/151/1. Financial support from the European Graduate School, Non-Equilibrium Phenomena and Phase Transition in Complex Systems, is also gratefully acknowledged. E. Brasselet, T. V. Galstian, and L. J. Dubé acknowledge financial support from the National Science and Engineering Research Canada.

E. Brasselet, the corresponding author, can be reached by e-mail at ebrassel@ens-lyon.fr. D. O. Krimer's e-mail address is Dmitry.Krimer@uni-bayreuth.de.

*Lorenz Kramer passed away on April 5, 2005.

†Also at Centre d'Optique, Photonique, et Laser, Université Laval, Québec, Canada G1K7P4.

‡Also at Laboratoire de Chimie-Physique-Matière et Rayonnement, Université Pierre et Marie Curie, 75231 Paris 05, France.

REFERENCES AND NOTES

1. N. V. Tabiryan, A. V. Sukhov, and B. Y. Zel'dovich, "Orientational optical nonlinearity of liquid-crystals," Mol. Cryst. Liq. Cryst. **136**, 1–139 (1986).
2. I. C. Khoo and S. T. Wu, *Optics and Nonlinear Optics of Liquid Crystals* (World Scientific, 1993).
3. E. Santamato, "Giant optical nonlinearities in nematic liquid crystals," in *Nonlinear Optical Material and Devices for Applications in Information Technology*, A. Miller, K. R. Welford, and B. Daino, eds. (Kluwer Academic, 1995), pp. 103–139.
4. F. Simoni, *Nonlinear Optical Properties of Liquid Crystals and Polymer Dispersed Liquid Crystals* (World Scientific, 1997).
5. G. Cipparrone, V. Carbone, C. Versace, C. Umeton, R. Bartolino, and F. Simoni, "Optically induced chaotic behavior in nematic liquid-crystal films," Phys. Rev. E **47**, 3741–3744 (1993).
6. G. Demeter and L. Kramer, "Transition to chaos via gluing

bifurcations in optically excited nematic liquid crystals," Phys. Rev. Lett. **83**, 4744–4747 (1999).
7. G. Demeter, "Complex nonlinear behavior in optically excited nematic liquid crystals," Phys. Rev. E **61**, 6678–6688 (2000).
8. G. Demeter and L. Kramer, "Numerical investigation of optically induced director oscillations in nematic liquid crystals," Phys. Rev. E **64**, 020701 (2001).
9. E. Brasselet, "Comment on 'Numerical investigation of optically induced director oscillations in nematic liquid crystals'," Phys. Rev. E (to be published).
10. A. Vella, A. Setaro, B. Piccirillo, and E. Santamato, "On–off intermittency in chaotic rotation induced in liquid crystals by competition between spin and orbital angular momentum of light," Phys. Rev. E **67**, 051704 (2003).
11. P. G. de Gennes and J. Prost, *The Physics of Liquid Crystals*, 2nd ed. (Clarendon, 1993).
12. A. S. Zolot'ko, V. F. Kitaeva, N. Kroo, N. N. Sobolev, and L. Csillag, "Light-induced Fréedericksz transition in an MBBA crystal," Pis'ma Zh. Eksp. Teor. Fiz. **34**, 263–267 (1981), [JETP Lett. **34**, 250–254 (1981)].
13. E. Santamato, B. Daino, M. Romagnoli, M. Settembre, and Y. R. Shen, "Collective rotation of molecules driven by the angular momentum of light in a nematic film," Phys. Rev. Lett. **57**, 2423–2426 (1986).
14. A. S. Zolot'ko and A. P. Sukhorukov, "Fréedericksz transition induced in nematic liquid-crystal by circularly polarized-light wave," Pis'ma Zh. Eksp. Teor. Fiz. **52**, 707–710 (1990) [JETP Lett. **52**, 62–65 (1990)].
15. L. Marrucci, G. Abbate, S. Ferraiuolo, P. Maddalena, and E. Santamato, "Self-stimulated light scattering in nematic liquid crystals: theory and experiment," Phys. Rev. A **46**, 4859–4868 (1992).
16. E. Brasselet, B. Doyon, T. V. Galstian, and L. J. Dubé, "New laser induced spatio-temporal transition in nematics," Phys. Lett. A **299**, 212–216 (2002).
17. D. O. Krimer, G. Demeter, and L. Kramer, "Orientational dynamics induced by circularly polarized light in nematic liquid crystals," Mol. Cryst. Liq. Cryst. Suppl. Ser. **421**, 117–131 (2004).
18. E. Santamato, G. Abbate, P. Maddalena, L. Marrucci, and Y. R. Shen, "Laser-induced nonlinear dynamics in a nematic liquid-crystal film," Phys. Rev. Lett. **64**, 1377–1380 (1990).
19. A. Vella, B. Piccirillo, and E. Santamato, "Coupled-mode approach to the nonlinear dynamics induced by an elliptically polarized laser field in liquid crystals at normal incidence," Phys. Rev. E **65**, 031706 (2002). We have found some misprints in this reference. In Eq. (20), $U_n(\cos z)$ should read $U_n(\cos u)$. Eq. (26) should read

$$\bar{\phi}_n = -\frac{\tilde{I}}{2n(n+2)}[\sin 2\chi\, A_n(\alpha) + \cos 2\chi \sin 2\phi_0 B_n(\alpha)].$$

The prefactor f_n in Eq. (27) should read as

$$f_n = -2\{\sin 2\chi[A_n(\alpha) - C_n(\alpha)] + \cos 2\chi \sin 2\phi_0[B_n(\alpha) + D_n(\alpha)]\},$$

and in Eq. (28), the integrals C_n and D_n should read as

$$C_n = \alpha\int_0^1 (1-v)\cos(\alpha v)U_n\{\cos[u(v)]\}\mathrm{d}v,$$

$$D_n = \alpha\int_0^1 (1-v)\sin(\alpha v)U_n\{\cos[u(v)]\}\mathrm{d}v.$$

20. A. S. Zolot'ko, V. F. Kitaeva, N. N. Sobolev, V. Y. Fedorovich, A. P. Sukhorukov, N. Kroo, and L. Csillag, "Polarization dynamics of an ordinary light wave interacting with a nematic liquid crystal," Liq. Cryst. **15**, 787–797 (1993).
21. E. Santamato, P. Maddalena, L. Marrucci, and B. Piccirillo, "Experimental study of the molecular reorientation induced by the ordinary wave in a nematic liquid crystal film," Liq. Cryst. **25**, 357–362 (1998).
22. V. Carbone, G. Cipparrone, and G. Russo, "Homoclinic gluing bifurcations during the light induced reorientation in nematic-liquid-crystal films," Phys. Rev. E **63**, 051701 (2001).
23. D. O. Krimer, G. Demeter, and L. Kramer, "Pattern-forming instability induced by light in pure and dye-doped nematic liquid crystals," Phys. Rev. E **66**, 031707 (2002).
24. B. Piccirillo, C. Toscano, F. Vetrano, and E. Santamato, "Orbital and spin photon angular momentum transfer in liquid crystals," Phys. Rev. Lett. **86**, 2285–2288 (2001).
25. B. Piccirillo, A. Vella, and E. Santamato, "Optical Fréedericksz transition in liquid crystals and transfer of the orbital angular momentum of light," Phys. Rev. E **69**, 021702 (2004).
26. For a classification of the different types of bifurcation, the reader is invited to consult, e.g., J. Guckenheimer and P. Holmes, *Nonlinear Oscillations, Dynamical Systems, and Bifurcation of Vector Fields* (Springer-Verlag, 1983). See also Refs. 27 and 28.
27. J. Hale and H. Koçak, *Dynamics and Bifurcations* (Springer-Verlag, 1991).
28. P. Glendinning, *Stability, Instability and Chaos* (Cambridge U. Press, 1996).
29. M. Abramowitz and I. A. Stegun, *Handbook of Mathematical Functions* (Dover, 1970).
30. B. Y. Zel'dovich and N. Tabiryan, "Theory of optically induced Fredericksz transition," Zh. Eksp. Teor. Fiz. **82**, 1126–1146 (1982) [Sov. Phys. JETP **55**, 656–666 (1982)].
31. E. Brasselet, T. V. Galstian, L. J. Dubé, D. O. Krimer, and L. Kramer, "Bifurcation analysis of optically induced dynamics in nematic liquid crystals: circular polarization at normal incidence," J. Opt. Soc. Am. B **22**, 1671–1680 (2005).
32. S. D. Durbin, S. M. Arakelian, and Y. R. Shen, "Laser-induced diffraction rings from a nematic-liquid-crystal film," Opt. Lett. **6**, 411–413 (1981).
33. E. Brasselet, B. Doyon, T. V. Galstian, and L. J. Dubé, "Optically induced dynamics in nematic liquid crystals: the role of finite beam size," Phys. Rev. E **69**, 021701 (2004).
34. The trajectory in the (n_x, n_y) plane is plotted at $z = L/2 - \ell(\ell \neq 0)$. The reason for this somewhat arbitrary value of z is to have contributions from all polar modes because, by construction, the even modes $\Theta_n \sin(n\pi z/L)$ are zero at the center of the cell ($z = L/2$).
35. The stable LD state in the present example (just above ρ_L for $\chi = 0.57$) is represented by a stable focus in that for lower values of χ the director settles to a LO state above the homoclinic bifurcation.
36. E. Brasselet and T. V. Galstian, "Optical multistability and confined orientational states in nematic liquid crystals: strong excitation regime," J. Opt. Soc. Am. B **18**, 982–988 (2001).